

H. Hosseini · N. Namazi

# Acoustic scattering of spherical waves incident on a long fluid-saturated poroelastic cylinder

Received: 14 November 2011 / Revised: 22 April 2012 / Published online: 28 June 2012  
© Springer-Verlag 2012

**Abstract** Acoustic scattering of spherical waves generated by a monopole point source in a perfect (inviscid and ideal) compressible fluid by a fluid-saturated porous cylinder of infinite length is studied theoretically in the present study. The formulation utilizes the Biot theory of dynamic poroelasticity along with the appropriate wave-field expansions, the translational addition theorem for spherical wave functions, and the pertinent boundary conditions to obtain a closed-form solution in the form of infinite series. The analytical results are illustrated with a numerical example in which a monopole point source within water is located near a porous cylinder with a water-saturated Ridgefield sandstone formation. The numerical results reveal the effects of source excitation frequency, the cylinder interface permeability condition, and the location of the point source and the field point on the backscattered pressure magnitudes. Limiting cases are considered, and the obtained numerical results are validated by already well-known solutions.

## 1 Introduction

The problem of acoustic scattering by cylindrical obstacles has been an interesting subject of investigations over the past few decades because of its broad applications in various scientific areas. The first pioneering study of the acoustic plane-wave scattering from submerged solid elastic cylinders is due to Faran [1]. He developed the scattering theory for a plane wave normally incident upon a solid elastic cylinder in a fluid medium by solving the wave equations in cylindrical coordinates and matching boundary conditions at the surface of the cylinder. Scattering of incident plane waves from a long solid or rigid cylindrical component has been studied extensively, and different analytical and numerical solutions have been developed. The investigations include multiple scattering [2], scattering by shells [3], rods [4], elliptic cylinders [5], layered cylinders [6], and the effects of the incidence angle [7,8], material anisotropy [9,10], resonance modes [11], existence of interface [12–14], and the acoustic backscattering enhancements [15]. Although most of these investigations are restricted to solid or rigid elastic cases, in recent researches there has been a progressing interest in considering the permeability of obstacles and finding the analytical solutions for acoustic scattering by cylindrical obstacles with porous formation. Mechel [16] studied scattering of the acoustic plane waves by porous absorbing cylinders and derived a formulation for the scattered sound field in series of Bessel functions. Scattering of ultrasonic plane waves by a fluid-saturated porous cylinder was examined by Laperre [17]. Umnova [18] studied the effects of porous covering on the sound attenuation by a finite periodic array of long

---

H. Hosseini  
Department of Mechanical Engineering, Aliabad Katoul Branch, Islamic Azad University, Aliabad Katoul, Iran

N. Namazi (✉)  
Department of Mechanical Engineering, Semnan Branch, Islamic Azad University, Semnan, Iran  
E-mail: nasirnamazi@gmail.com  
Tel.: +98-17-22291693; +98-09-111798454  
Fax: +98-17-36237935

rigid cylinders. Hasheminejad [19] studied the interaction of a plane compressional sound wave with a cluster of two fluid-saturated porous elastic cylinders submerged in an unbounded acoustic medium. He also studied acoustic plane-wave scattering from an infinitely long fluid-saturated poroelastic cylinder located near a planar boundary with locally varying surface impedance [20]. The dynamic response of a cylindrical cavity in an infinite cross-anisotropic porous medium has been studied by Gatmiri [21]. Zhou [22] developed a semi analytical method to solve the scattering of plane waves by a circular pipeline embedded in an infinite poroelastic medium. Ogam et al. modeled the ultrasonic propagation in cancellous bone using modified Biot theory (MBT) and studied the ultrasonic characterization of human cancellous bone samples by solving the inverse problem using experimental transmitted signals [23]. Also a method based on theory and experiment of diffraction of acoustic plane waves by an air-saturated porous cylinder with rigid frame in the audible frequency regime has been developed by Ogam et al. [24]. In addition, they have developed an acoustic method for the recovery of the material parameters of a rigid frame, air-saturated polymeric foam cylinder [25], and also they have developed a wave-fluid-saturated poroelastic structure interaction model based on the MBT and plane-wave decomposition using orthogonal cylindrical functions [26]. Osman [27] has presented an analytical solution for the response of a poroelastic medium around a laterally loaded rigid cylinder using Biot's consolidation theory.

In contrast to the numerous works which treat the scattering of plane waves, there are very few theoretical analyses relating the scattering of spherical sound waves by long cylindrical components. Piquette [28] investigated the problem of the scattering of spherical sound waves by a long rigid cylinder and showed that an approximate solution for the scattered pressure can be derived by assuming one of the vector potential components equal to zero. Li and Ueda [29] showed that the scattering of a spherical wave by a solid cylinder of infinite length can be directly formulated by using the already known solutions for plane-wave incident, and moreover, some more analytical results were obtained for the amplitude of a spherical wave backscattered from a solid cylinder immersed in water by Sheng [30]. Recently, Lui and Li [31] have investigated the scattering of spherical sound waves by an infinitely long solid cylinder above an impedance boundary both theoretically and experimentally and in addition they have derived the total far-field scattered pressure. Also Chen [32] has used the addition theorem and superposition techniques to solve the problem of wave scattering by multiple circular cylinders in the wave field generated by the point sound sources. Hasheminejad and Hosseini employed the cylindrical/spherical wave-field transformations to investigate harmonic acoustic radiation from a modally oscillating spherical source positioned at the center of a fluid-filled cylindrical cavity embedded within a fluid-saturated poroelastic formation [33,34].

In this study, we employ the Biot theory of dynamic poroelasticity and appropriate acoustic field equations as well as pertinent boundary conditions to carry out an analysis for the scattering of acoustic sound waves due to a monopole point source immersed in an inviscid fluid by a fluid-saturated porous cylinder of infinite length. In order to present the general behavior of the obtained solution, we consider a numerical example in which a porous cylinder with water-saturated Ridgefield sandstone formation is placed near a monopole point source embedded in water. Primary attention is focused on studying the effects of incident wave frequency, solid/fluid interface permeability condition, the location of the point source, and the coordinates of the field point on the backscattered pressure magnitudes.

This article is arranged as follows. Section 2 gives the theoretical development for the acoustic field backscattered from a cylindrical obstacle excited by a monopole point source. A poroelastic model of the problem using Biot's theory is developed in Sect. 2.2, and the equations related to the propagation of the acoustic waves in a porous cylinder are presented as well. Finally, the solution is obtained by imposing appropriate boundary conditions at the fluid/solid interface. The analytical results are illustrated with a numerical example in Sect. 3, and the conclusion is given in Sect. 4.

## 2 Formulation

### 2.1 Basic acoustic field equations

The geometry and the coordinate system of the general problem are given in Fig. 1. We consider an infinitely long cylinder of radius  $a$ , with poroelastic formation immersed in a perfect (inviscid and ideal) compressible fluid of density  $\rho_0$  and sound speed  $c_0$ . It is assumed that the origin of the cylindrical coordinates  $(R, \theta, Z)$  is placed on the symmetry axis of the porous cylinder. The monopole point source with angular frequency  $\omega$  is placed exterior to the cylinder at the point  $S$  with cylindrical coordinates  $(d, \pi, 0)$ , and the field point  $D$  is situated at the cylindrical coordinates  $(R, \theta, Z)$ .

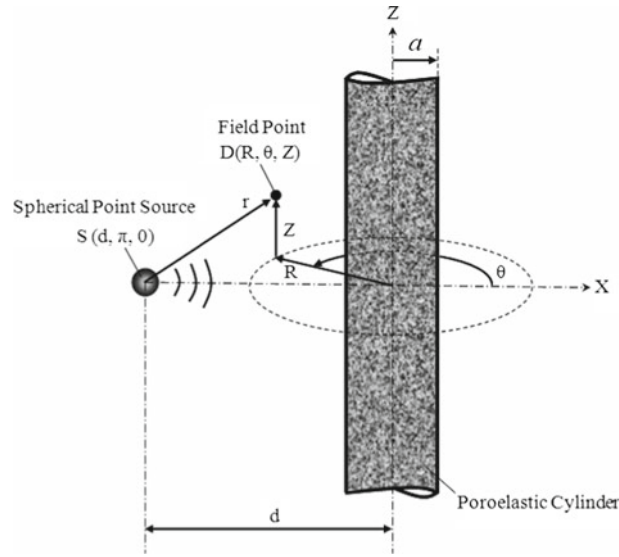


**Fig. 1** Problem geometry

The basic field equations in the fluid may conveniently be expressed in terms of a scalar velocity potential  $\varphi$  as [35]

$$\dot{\mathbf{s}} = \nabla \varphi \quad p = -\rho_0 \dot{\varphi}, \quad (1)$$

where  $\dot{\mathbf{s}}$  is the fluid particle velocity vector (over-dot denotes differentiation with respect to time) and  $p$  is the acoustic pressure. Applying Fourier transformation with respect to time (frequency):

$$\tilde{g}(\omega) = \int_{-\infty}^{+\infty} g(t) e^{-i\omega t} dt, \quad g(t) = \frac{1}{2\pi} \int_{-\infty}^{+\infty} \tilde{g}(\omega) e^{i\omega t} d\omega, \quad (2)$$

where  $g(t)$  is an arbitrary function of time, leads to

$$-i\omega \tilde{\mathbf{s}} = \nabla \tilde{\varphi}, \quad \tilde{p} = i\omega \rho_0 \tilde{\varphi}, \quad (3)$$

where  $\tilde{\varphi} = \tilde{\varphi}_s + \tilde{\varphi}_c$  satisfies the classical Helmholtz equation  $\nabla^2 \tilde{\varphi} + k^2 \tilde{\varphi} = 0$ , in which  $k = \omega/c_0$  is the acoustic wave number and  $\tilde{\varphi}_s$  is the incident spherical wave in the fluid which can simply be expressed as follows [31]:

$$\tilde{\varphi}_s = -\frac{Q_s}{4\pi} \frac{e^{ikr}}{r}, \quad (4)$$

where  $r$  is the radial distance from the point source and  $Q_s$  is the source strength. Using the addition theorem to  $\tilde{\varphi}_s$ , it can be expressed in terms of the cylindrical coordinates  $(R, \theta, Z)$  centered on the axis of the porous cylinder as [29]:

$$\tilde{\varphi}_{s/c} = \sum_{n=0}^{\infty} \int_{-\infty}^{+\infty} \frac{Q_s}{4\pi} (-1)^n \frac{i}{2} \varepsilon_n J_n(\gamma R) H_n(\gamma d) \cos(n\theta) e^{i\zeta Z} d\zeta, \quad (5)$$

where  $\varepsilon_n$  is the Neumann factor ( $\varepsilon_0 = 1$  and  $\varepsilon_n = 2$  for  $n > 0$ ),  $J_n$  is the cylindrical Bessel function of the first kind of order  $n$ ,  $H_n$  is the cylindrical Hankel function of the first kind of order  $n$ , and  $\gamma = \sqrt{k^2 - \zeta^2}$ .

The corresponding scattered cylindrical wave  $\tilde{\varphi}_c$  at an arbitrary field point  $D$  in the fluid medium has the following form [31]:

$$\tilde{\varphi}_c = \sum_{n=0}^{\infty} \int_{-\infty}^{+\infty} A_n H_n(\gamma R) \cos(n\theta) e^{i\zeta Z} d\zeta, \quad (6)$$

in which  $A_n$  are the unknown scattering coefficients which can be determined by imposing the appropriate boundary conditions on the surface of the cylinder.

## 2.2 Poroelastic model

Before proceeding to analyze the full problem, we shall first briefly review the salient features of Biot's theory of wave propagation in poroelastic materials. On a microscopic scale, sound propagation in porous materials is generally difficult to study due to the complicated geometries of the frames. In Biot's model [36,37], the medium is taken to be a macroscopically homogeneous and isotropic two-component solid/fluid system with the same macroscopic bulk properties as the real porous material. Denoting the average macroscopic displacement of the solid frame and the saturating fluid on the elementary macroscopic volume (EMV) by the vectors  $\mathbf{u}$  and  $\mathbf{U}$ , respectively, the macroscopic stress tensor  $\sigma_{ij}$  and the mean pore fluid pressure  $p_p$  are given by [38]

$$\sigma_{ij} = (\lambda_f e - \beta M \xi) \delta_{ij} + 2\mu e_{ij}, \quad p_p = M(\xi - \beta e), \quad (7)$$

where  $\delta_{ij}$  is the Kronecker symbol ( $\delta_{ij} = 0$  for  $i \neq j$  and  $\delta_{ij} = 1$  for  $i = j$ ), and

$$\begin{aligned} \lambda_f &= K_f - \frac{2}{3}\mu, \quad M = 1/[(\beta - \phi_0)/K_s + \phi_0/K_\Pi], \quad e_{ij} = (u_{i,j} + u_{j,i})/2, \\ \beta &= 1 - K_o/K_s, \quad \xi = -\nabla \cdot \mathbf{w} = -\phi_0(\varepsilon - e), \quad e = \nabla \cdot \mathbf{u}, \quad \varepsilon = \nabla \cdot \mathbf{U}, \\ K_f &= \frac{\phi_0(1/K_s - 1/K_\Pi) + 1/K_s - 1/K_o}{\phi_0/K_o(1/K_s - 1/K_\Pi) + 1/K_s(1/K_s - 1/K_o)}, \end{aligned} \quad (8)$$

in which  $\mu$  is the shear modulus of the bare skeletal frame,  $\phi_0$  the pore volume fraction (porosity),  $K_o$  the bulk modulus of the dry skeleton,  $K_s$  the bulk modulus of the material constituting the elastic matrix,  $K_\Pi$  the bulk modulus of the saturating fluid,  $K_f$  the bulk modulus of the closed system, and  $\mathbf{w} = \phi_0(\mathbf{U} - \mathbf{u})$  is the filtration displacement vector.

The coupled equations of motion governing the displacements of the solid matrix and interstitial liquid, with dissipation taken into account, are [38]

$$\begin{aligned} (\lambda + 2\mu)\nabla\nabla \cdot \mathbf{u} + Q\nabla\nabla \cdot \mathbf{U} - \mu\nabla \times \nabla \times \mathbf{u} &= \rho_{11}\ddot{\mathbf{u}} + \rho_{12}\ddot{\mathbf{U}} + b(t) * (\dot{\mathbf{u}} - \dot{\mathbf{U}}), \\ Q\nabla\nabla \cdot \mathbf{u} + \phi_0^2 M \nabla\nabla \cdot \mathbf{U} &= \rho_{12}\ddot{\mathbf{u}} + \rho_{22}\ddot{\mathbf{U}} - b(t) * (\dot{\mathbf{u}} - \dot{\mathbf{U}}), \end{aligned} \quad (9)$$

where

$$\begin{aligned} \lambda &= \lambda_f + \phi_0 M(\phi_0 - 2\beta), & \rho_{11} &= \rho + \phi_0 \rho_\Pi(\alpha - 2), \\ Q &= \phi_0 M(\beta - \phi_0), & \rho_{12} &= \phi_0 \rho_\Pi(1 - \alpha), \\ \rho &= (1 - \phi_0)\rho_s + \phi_0 \rho_\Pi, & \rho_{22} &= \rho - \rho_{11} - 2\rho_{12} = \alpha\phi_0 \rho_\Pi, \end{aligned}$$

in which  $\rho_s$  is the density of the solid matrix,  $\rho_\Pi$  the density of the saturating fluid,  $\rho$  the total mass density of the fluid-saturated material,  $\alpha$  the tortuosity of the porous medium, and the effective densities  $\rho_{11}$ ,  $\rho_{12}$ ,  $\rho_{22}$  are frequency-independent parameters relying on the geometry of the porous medium and the density of the saturating fluid. In Biot's theory at low frequencies, the fluid flow  $(\mathbf{U} - \mathbf{u})$  relative to the solid phase is assumed to be of Poiseuille type, and the viscous drag forces dominate the flow. At higher frequencies, a boundary layer develops on the solid phase surfaces and the inertial forces dominate the flow, so Poiseuille flow assumption does not hold. The quantity  $b(t)$  is a viscous coupling factor that accounts for the combined effects of macroscopic frictional dissipation due to finite fluid viscosity (viscous drag forces) and the interaction between the fluid and solid movements (inertial forces). A star between two variables represents time convolution [39].

The Helmholtz decomposition theorem allows us to resolve the displacement fields as superposition of longitudinal and transverse vector components,

$$\mathbf{u} = \nabla\phi + \nabla \times \boldsymbol{\psi}, \quad \mathbf{U} = \nabla\chi + \nabla \times \boldsymbol{\Theta}, \quad (10)$$

where  $\boldsymbol{\psi} = \psi \mathbf{e}_Z + \nabla \times W \mathbf{e}_Z$  and  $\boldsymbol{\Theta} = \Theta \mathbf{e}_Z + \nabla \times X \mathbf{e}_Z$ . Substituting the above resolutions into Biots' field equations of motion (9) and subsequent application of Fourier transformation (2) with respect to the time variable yields

$$\begin{aligned} (\lambda + 2\mu)\nabla^2 \tilde{\phi} + Q\nabla^2 \tilde{\chi} &= [\omega^2 \rho_{11} - i\omega \tilde{b}(\omega)] \tilde{\phi} + [\omega^2 \rho_{12} + i\omega \tilde{b}(\omega)] \tilde{\chi}, \\ Q\nabla^2 \tilde{\phi} + \phi_0^2 M \nabla^2 \tilde{\chi} &= [\omega^2 \rho_{12} + i\omega \tilde{b}(\omega)] \tilde{\phi} + [\omega^2 \rho_{22} - i\omega \tilde{b}(\omega)] \tilde{\chi}, \\ \mu \nabla^2 \tilde{\psi} &= [\omega^2 \rho_{11} - i\omega \tilde{b}(\omega)] \tilde{\psi} + [\omega^2 \rho_{12} + i\omega \tilde{b}(\omega)] \tilde{\Theta}, \\ [\omega^2 \rho_{12} + i\omega \tilde{b}(\omega)] \tilde{\psi} &+ [\omega^2 \rho_{22} - i\omega \tilde{b}(\omega)] \tilde{\Theta} = 0. \end{aligned} \quad (11)$$

A very simple and fairly accurate model for the description of the coupling factor in the frequency domain is given by  $\tilde{b}(\omega) = \phi_0^2 \eta / \kappa \sqrt{1 - 4\alpha^2 \kappa^2 \rho_{\text{fl}} \omega / \eta \Lambda^2 \phi_0^2}$  in [40] where  $\kappa$  is the absolute permeability of the porous medium,  $\eta$  is the saturating fluid viscosity, and  $\Lambda \approx \sqrt{8\alpha\kappa/\phi_0}$  is the viscous characteristic length. Furthermore, after some manipulations on the potential equations (11), we arrive at the Helmholtz equation [34]:

$$\nabla^2 \tilde{\phi}_{f,s} + k_{f,s}^2 \tilde{\phi}_{f,s} = 0, \quad \nabla^2 \tilde{\psi} + k_t^2 \tilde{\psi} = 0, \quad \nabla^2 \tilde{W} + k_t^2 \tilde{W} = 0 \quad (12)$$

where  $k_f$ ,  $k_s$ , and  $k_t$  which designate the complex wave numbers of the fast compressional, slow compressional, and the elastic shear waves, respectively, are given as

$$k_{f,s}^2 = \frac{B \mp \sqrt{B^2 - 4AC}}{2A}, \quad k_t^2 = \frac{C}{\mu [\omega^2 \rho_{22} + i\omega \tilde{b}(\omega)]} \quad (13)$$

where

$$\begin{aligned} A &= (\lambda + 2\mu)\phi_0^2 M - Q^2, \quad C = \omega^2 [\omega^2 (\rho_{11}\rho_{22} - \rho_{12}^2) + i\omega \rho \tilde{b}(\omega)], \\ B &= \omega^2 [\rho_{11}\phi_0^2 M + \rho_{22}(\lambda + 2\mu) - 2\rho_{12}Q] + i\omega \tilde{b}(\omega)(\lambda + 2\mu + 2Q + \phi_0^2 M), \end{aligned} \quad (14)$$

and  $\nabla^2 = \frac{1}{R} \frac{\partial}{\partial R} (R \frac{\partial}{\partial R}) + \frac{1}{R^2} \frac{\partial^2}{\partial \theta^2} + \frac{\partial^2}{\partial z^2}$ . Furthermore, with some manipulations, the potentials  $\tilde{\phi}$ ,  $\tilde{\chi}$ ,  $\tilde{\Theta}$ , and  $\tilde{\psi}$  may be expressed as

$$\tilde{\phi} = \tilde{\phi}_f + \tilde{\phi}_s, \quad \tilde{\chi} = \mu_f \tilde{\phi}_f + \mu_s \tilde{\phi}_s, \quad \tilde{\Theta} = \alpha_0 \tilde{\psi} \quad (15)$$

where

$$\begin{aligned} \mu_{f,s} &= \frac{\omega^2 (\rho_{11}\phi_0^2 M - \rho_{12}Q) - k_{f,s}^2 [(\lambda + 2\mu)\phi_0^2 M - Q^2] + i\omega \tilde{b} (Q + \phi_0^2 M)}{\omega^2 (\rho_{22}Q - \rho_{12}\phi_0^2 M) + i\omega \tilde{b}(\omega) (Q + \phi_0^2 M)}, \\ \alpha_0 &= -\frac{\omega^2 \rho_{12} - i\omega \tilde{b}(\omega)}{\omega^2 \rho_{22} + i\omega \tilde{b}(\omega)}. \end{aligned} \quad (16)$$

Also, the solid and liquid displacements in  $R$ -,  $\theta$ -, and  $Z$ -directions in terms of displacement potentials in the poroelastic cylinder are written as

$$\tilde{u}_R = \frac{\partial \tilde{\phi}}{\partial R} + \frac{\partial \tilde{\psi}}{R \partial \theta} + \frac{\partial^2 \tilde{W}}{\partial R \partial Z}, \quad \tilde{u}_\theta = \frac{\partial \tilde{\phi}}{R \partial \theta} - \frac{\partial \tilde{\psi}}{\partial R} + \frac{\partial^2 \tilde{W}}{R \partial \theta \partial Z}, \quad \tilde{u}_Z = \frac{\partial \tilde{\phi}}{\partial Z} - \nabla^2 \tilde{W} + \frac{\partial^2 \tilde{W}}{\partial Z^2}, \quad (17.1-3)$$

$$\tilde{U}_R = \frac{\partial \tilde{\chi}}{\partial R} + \frac{\partial \tilde{\Theta}}{R \partial \theta} + \frac{\partial^2 \tilde{X}}{\partial R \partial Z}, \quad \tilde{U}_\theta = \frac{\partial \tilde{\chi}}{R \partial \theta} - \frac{\partial \tilde{\Theta}}{\partial R} + \frac{\partial^2 \tilde{X}}{R \partial \theta \partial Z}, \quad \tilde{U}_Z = \frac{\partial \tilde{\chi}}{\partial Z} - \nabla^2 \tilde{X} + \frac{\partial^2 \tilde{X}}{\partial Z^2}. \quad (17.4-6)$$

Moreover, the expressions for the frame and liquid dilatation can be manipulated to yield

$$\begin{aligned} e &= \nabla \cdot \tilde{\mathbf{u}} = \nabla^2 \tilde{\phi} = \nabla^2 \tilde{\phi}_f + \nabla^2 \tilde{\phi}_s = -k_f^2 \tilde{\phi}_f - k_s^2 \tilde{\phi}_s, \\ \varepsilon &= \nabla \cdot \tilde{\mathbf{U}} = \nabla^2 \tilde{\chi} = \mu_f \nabla^2 \tilde{\phi}_f + \mu_s \nabla^2 \tilde{\phi}_s = -\mu_f k_f^2 \tilde{\phi}_f - \mu_s k_s^2 \tilde{\phi}_s. \end{aligned} \quad (18)$$

Lastly, utilizing Eqs. (7), (8), (15) and (18), the pore fluid pressure and the relevant stress components are expressed as

$$\tilde{p}_p = Mb_f k_f^2 \tilde{\phi}_f + Mb_s k_s^2 \tilde{\phi}_s, \quad (19.1)$$

$$\tilde{\sigma}_{RR} = a_f k_f^2 \tilde{\phi}_f + a_s k_s^2 \tilde{\phi}_s + 2\mu \left( \frac{\partial \tilde{u}_R}{\partial R} \right), \quad (19.2)$$

$$\tilde{\sigma}_{RZ} = \mu \left( \frac{\partial \tilde{u}_R}{\partial Z} + \frac{\partial \tilde{u}_Z}{\partial R} \right), \quad (19.3)$$

$$\tilde{\sigma}_{R\theta} = \frac{\mu}{R} \left( R \frac{\partial \tilde{u}_\theta}{\partial R} - \tilde{u}_\theta + \frac{\partial \tilde{u}_R}{\partial \theta} \right), \quad (19.4)$$

where

$$a_{f,s} = -\lambda_f + \phi_0 \beta M (1 - \mu_{f,s}), \quad b_{f,s} = \beta + \phi_0 (\mu_{f,s} - 1). \quad (20)$$

Now, the general solutions of Eqs. (12), corresponding to the fast dilatational, slow dilatational, and shear waves transmitted into the cylindrical poroelastic medium are, respectively, written in the cylindrical coordinate system as [34]:

$$\begin{aligned} \tilde{\phi}_f(R, \theta, Z) &= \sum_{n=0}^{\infty} \int_{-\infty}^{+\infty} B_n J_n(\gamma_f R) \cos(n\theta) e^{i\zeta Z} d\zeta, \\ \tilde{\phi}_s(R, \theta, Z) &= \sum_{n=0}^{\infty} \int_{-\infty}^{+\infty} C_n J_n(\gamma_s R) \cos(n\theta) e^{i\zeta Z} d\zeta, \\ \tilde{W}(R, \theta, Z) &= \sum_{n=0}^{\infty} \int_{-\infty}^{+\infty} D_n J_n(\gamma_t R) \cos(n\theta) e^{i\zeta Z} d\zeta, \\ \tilde{X}(R, \theta, Z) &= \sum_{n=0}^{\infty} \int_{-\infty}^{+\infty} E_n J_n(\gamma_t R) \sin(n\theta) e^{i\zeta Z} d\zeta \end{aligned} \quad (21)$$

where  $\gamma_{f,s,t} = \sqrt{k_{f,s,t}^2 - \zeta^2}$ , and  $B_n, C_n, D_n, E_n$  are unknown transmission coefficients which will be determined later by application of the boundary conditions.

### 2.3 Boundary conditions

The appropriate set of the boundary conditions which have to be satisfied in the Fourier space and at the fluid–solid interface (i.e.,  $R = a$ ) is [34]:

- (i) compatibility of the normal stress of the porous cylinder with the acoustic pressure in the fluid

$$\tilde{\sigma}_{RR} + \tilde{p} = 0, \quad (22.1)$$

- (ii) consistency of the pressure drop and the normal component of the filtration velocity

$$-i\omega \tilde{w}_R = -\kappa_s (\tilde{p} - \tilde{p}_p), \quad (22.2)$$

- (iii) continuity of the normal component of the filtration velocity

$$\tilde{w}_R = \phi_0 (\tilde{U}_R - \tilde{u}_R) = \tilde{s}_R - \tilde{u}_R, \quad (22.3)$$

(iv) vanishing of circumferential and axial stress components at the surface of the cylinder

$$\tilde{\sigma}_{R\theta} = 0, \quad (22.4)$$

$$\tilde{\sigma}_{RZ} = 0, \quad (22.5)$$

where the parameter  $\kappa_s$  characterizes the permeability of the interface. For an open interface, we expect zero pressure drop ( $p = p_p$ ), and hence we let  $\kappa_s = \infty$ . To characterize a sealed interface (i.e., for  $\dot{\mathbf{w}} = 0$ ), we take  $\kappa_s = 0$ .

In order to satisfy the boundary condition (22.1), we need to express the total acoustic pressure in the fluid in the cylindrical coordinate system, that is, we set

$$\begin{aligned} \tilde{p}(R, \theta, Z) &= i\rho_0\omega(\tilde{\varphi}_{s/c} + \tilde{\varphi}_c), \\ \tilde{p}(R, \theta, Z) &= i\rho_0\omega \sum_{n=0}^{\infty} \int_{-\infty}^{\infty} \left\{ \frac{Q_s}{4\pi} (-1)^n \frac{i}{2} \varepsilon_n J_n(\gamma R) H_n(\gamma d) + A_n H_n(\gamma R) \right\} \cos(n\theta) e^{i\zeta Z} d\zeta. \end{aligned} \quad (23)$$

Also, using Eq. (21) along with Eq. (17.1) in Eq. (19.2), the total radial stress induced in the porous cylinder in the cylindrical coordinate system can be written as

$$\begin{aligned} \tilde{\sigma}_{RR}(R, \theta, Z) &= \sum_{n=0}^{\infty} \int_{-\infty}^{+\infty} \left\{ \left[ a_f k_f^2 J_n(\gamma_f R) + 2\mu\gamma_f^2 J_n''(\gamma_f R) \right] B_n + \left[ a_s k_s^2 J_n(\gamma_s R) + 2\mu\gamma_s^2 J_n''(\gamma_s R) \right] C_n \right. \\ &\quad \left. + \left[ i2\mu\zeta \gamma_t^2 J_n''(\gamma_t R) \right] D_n + \frac{2\mu n}{R^2} \left[ \gamma_t R J_n'(\gamma_t R) - J_n\{\gamma_t R\} \right] E_n \right\} \cos(n\theta) e^{i\zeta Z} d\zeta. \end{aligned} \quad (24)$$

Substitution of Eqs. (23) and (24) into Eq. (22.1), and subsequent inverse Fourier transformation with respect to the  $Z$ -parameter leads to the following expression for the first boundary condition (22.1) on the surface of the cylinder:

$$\begin{aligned} &[i\rho_0\omega H_n(\gamma a)] A_n + \left[ a_f k_f^2 J_n(\gamma_f a) + 2\mu\gamma_f^2 J_n''(\gamma_f a) \right] B_n + \left[ a_s k_s^2 J_n(\gamma_s a) + 2\mu\gamma_s^2 J_n''(\gamma_s a) \right] C_n \\ &+ \left[ i2\mu\zeta \gamma_t^2 J_n''(\gamma_t a) \right] D_n + \frac{2\mu n}{a^2} \left[ \gamma_t a J_n'(\gamma_t a) - J_n\{\gamma_t a\} \right] E_n = \frac{\rho_0\omega Q_s}{8\pi} (-1)^n \varepsilon_n J_n(\gamma a) H_n(\gamma d). \end{aligned} \quad (25.1)$$

Similarly, applying the above procedure to the boundary conditions (22.2–22.5) leads to

$$\begin{aligned} &[i\rho_0\omega\kappa_s H_n(\gamma a)] A_n + \left[ i(1 - \mu_f)\omega\phi_0\gamma_f J_n'(\gamma_f a) - \kappa_s b_f M k_f^2 J_n(\gamma_f a) \right] B_n \\ &+ \left[ i(1 - \mu_s)\omega\phi_0\gamma_s J_n'(\gamma_s a) - \kappa_s b_s M k_s^2 J_n(\gamma_s a) \right] C_n + \left[ \omega\phi_0\zeta \gamma_t J_n'(\gamma_t a)(\alpha_0 - 1) \right] D_n \\ &+ \left[ \frac{i\omega\phi_0 n}{a} J_n(\gamma_t a)(1 - \alpha_0) \right] E_n = \frac{\rho_0\omega Q_s}{8\pi} (-1)^n \varepsilon_n \kappa_s J_n(\gamma a) H_n(\gamma d), \end{aligned} \quad (25.2)$$

$$\begin{aligned} &[-\gamma H_n'(\gamma a)] A_n + \left[ i\omega\gamma_f J_n'(\gamma_f a)(\phi_0(1 - \mu_f) - 1) \right] B_n \\ &+ \left[ i\omega\gamma_s J_n'(\gamma_s a)(\phi_0(1 - \mu_s) - 1) \right] C_n + \omega\zeta \gamma_t J_n'(\gamma_t a) [1 - \phi_0(1 - \alpha_0)] D_n \\ &+ \left[ \frac{i\omega n}{a} J_n(\gamma_t a)(\phi_0(1 - \alpha_0) - 1) \right] E_n = \frac{iQ_s}{8\pi} (-1)^n \varepsilon_n \gamma J_n'(\gamma a) H_n(\gamma d), \end{aligned} \quad (25.3)$$

$$\begin{aligned} &[2n(J_n(\gamma_f a) - \gamma_f a J_n'(\gamma_f a))] B_n + [2n(J_n(\gamma_s a) - \gamma_s a J_n'(\gamma_s a))] C_n \\ &+ [i2n\zeta(J_n(\gamma_t a) - \gamma_t a J_n'(\gamma_t a))] D_n \\ &+ [-\gamma_t^2 a^2 J_n''(\gamma_t a) + \gamma_t a J_n'(\gamma_t a) - n^2 J_n(\gamma_t a)] E_n = 0, \end{aligned} \quad (25.4)$$

$$\begin{aligned} &[i2\xi\gamma_f a^3 J_n'(\gamma_f a)] B_n + [i2\xi\gamma_s a^3 J_n'(\gamma_s a)] C_n \\ &+ [-\gamma_t^3 a^3 J_n'''(\gamma_t a) - \gamma_t^2 a^2 J_n''(\gamma_t a) + (-\xi^2 a^2 + 1 + n^2)\gamma_t a J_n'(\gamma_t a) - 2n^2 J_n(\gamma_t a)] D_n \\ &+ [ina^2 \xi J_n(\gamma_t a)] E_n = 0. \end{aligned} \quad (25.5)$$



Now, we can arrange Eqs. (22.1)–(22.5) in a matrix form,

$$\begin{pmatrix} a_{11} & a_{12} & a_{13} & a_{14} & a_{15} \\ a_{21} & a_{22} & a_{23} & a_{24} & a_{25} \\ a_{31} & a_{32} & a_{33} & a_{34} & a_{35} \\ 0 & a_{42} & a_{43} & a_{44} & a_{45} \\ 0 & a_{52} & a_{53} & a_{54} & a_{55} \end{pmatrix} \begin{pmatrix} A_n \\ B_n \\ C_n \\ D_n \\ E_n \end{pmatrix} = \begin{pmatrix} c_1 \\ c_2 \\ c_3 \\ 0 \\ 0 \end{pmatrix}, \quad (26)$$

where the pertinent expressions for the coefficients  $a_{ij}$  and  $c_i$  are provided in the “Appendix.” Consequently, by applying the standard method of Gaussian elimination, the linear system of Eq. (26) can be solved for the unknown coefficients. This completes the analysis of the problem. Next, we consider some numerical examples.

### 3 Results and discussion

In order to illustrate the nature and general behavior of the solution, we consider a numerical example in this section. Realizing the large number of parameters involved here while keeping in mind the availability of the numerical data for fluid-saturated porous materials, we confine our attention to a particular model. The ambient fluid is assumed to be water at atmospheric pressure and 300 K ( $\rho_0 = 1,000 \text{ kg/m}^3$ ,  $c_0 = 1,500 \text{ m/s}$ ), the porous cylinder is supposed to be of radius  $a = 10 \text{ cm}$ , and the source strength is  $Q_s = 0.1\pi \text{ m}^3/\text{s}$ . The input parameter values for water-saturated Ridgefield sandstone [41], which are used in the calculations, are compiled in Table 1.

Accurate computation of the Bessel functions is achieved by employing the Mathematica (7) specialized math functions “BesselJ” and “HankelH1.” The precision of the calculated values was checked against the printed tabulations in the handbook by Abramowitz and Stegun [42]. A Mathematica code was constructed for treating boundary conditions to determine the unknown coefficients and to compute the scattered pressure magnitudes as functions of the non-dimensional frequency ( $ka$ ) and the distance parameters  $\frac{Z}{a}$ ,  $\frac{d}{a}$  and  $\theta$ . Accurate computations for derivatives of Bessel functions were accomplished by utilizing (10.1.19) and (10.1.22) in [42]. In Biot’s theory, two frequency ranges are distinguished. At low-frequency range, the viscous forces, and at high-frequency range, the inertial forces dominate the fluid flow through the porous media. Biot limited the low-frequency range with a characteristic frequency  $f_c (\text{Hz}) = \frac{\phi_0 \eta}{2\pi \rho_0 \kappa \alpha}$ . For water-saturated Ridgefield sandstone which is considered as the fluid-saturated poroelastic cylinder in calculations,  $f_c = 1,346 \text{ Hz}$  [41] that corresponds to a non-dimensional frequency  $ka = 0.56$ , so at frequencies below  $f_c$ , the low-frequency regime and above it the high-frequency regime is dominant.

The computations were performed with a truncation constant of ( $N = 15$ ) to assure convergence in the high-frequency range. The truncation constant,  $N$ , used in evaluating the series is  $N = ka_{\max} + 5$  where  $ka_{\max}$  is the maximum value of the non-dimensional frequency,  $ka$ , on the graphs. This number of modes guarantees the correctness of the obtained results for the considered range of frequencies [43]. In addition, the convergence of the obtained numerical results for the truncation constant,  $N = 15$ , is checked with a second-decimal place accuracy.

Moreover, in order to properly evaluate the infinite integrals arising in the computations, keeping in mind that ( $\zeta = k$ ) is a singular point of the integrands, the interval of integration is divided into two separate regions: ( $0 \leq \zeta < k$ ), and ( $k < \zeta < \infty$ ).

**Table 1** Biot input parameter values

Parameter	Ridgefield sandstone	Unconsolidated sand	Nivelsteiner sandstone
$\phi_0$	0.37	0.44	0.33
$\alpha$	1.58	1.63	2.015
$\kappa (\text{m}^2)$	$27.7 \times 10^{-12}$	$1.1 \times 10^{-10}$	$5 \times 10^{-12}$
$\mu (\text{N/m}^2)$	$2.89 \times 10^{10}$	$6 \times 10^6$	$(4.55 - 0.227i) \times 10^9$
$K_{\text{fl}} (\text{N/m}^2)$	$2.55 \times 10^9$	$2.55 \times 10^9$	$2.223 \times 10^9$
$\Lambda (\text{m})$	$19.4 \times 10^{-6}$	$5.7 \times 10^{-5}$	$9 \times 10^{-8}$
$\rho_s (\text{kg/m}^3)$	2,500	2,650	2,650
$K_s (\text{N/m}^2)$	$4.99 \times 10^{10}$	$35 \times 10^9$	$36 \times 10^9$
$K_o (\text{N/m}^2)$	$5.24 \times 10^9$	$1.25 \times 10^7$	$(6.21 - 0.207i) \times 10^9$
$\rho_{\text{fl}} (\text{kg/m}^3)$	1,000	1,000	1,000
$\eta (\text{kg/ms})$	0.001	0.001	0.001



Subsequently, in intervals not including the singular points, the usual numerical integration methods such as trapezoidal and Simpson rules with small integration steps are employed to evaluate the integrals. Near the singularity, the numerical integrations are conducted by making use of the Gauss quadrature technique. The convergence of the numerical integrations is systematically secured by increasing the value of the upper limits of the integrals while looking for steadiness or stability in the numerical values of the integrals. The quantity that is used to present the numerical results for the scattered field is the relative scattered pressure which is defined as:

$$\text{Relative scattered pressure} = \left| \frac{P_{\text{scat}}}{P_{\text{ref}}} \right|, \quad (27)$$

where  $P_{\text{scat}}$  is the scattered pressure which is calculated at the field point  $D = (R, \theta, Z)$  and  $P_{\text{ref}}$  is the reference pressure which is calculated at 1m from the point source in the absence of the porous cylinder (incident free-field pressure). Also, as most of the acoustic experimental techniques are highly sensitive to the permeability of the interface, it seems logical to investigate the effect of the interface conditions on the scattered pressures. As mentioned before, this effect may be studied by making use of the parameter  $0 < \kappa_s < \infty$ , which characterizes the permeability of the interface. To avoid complications of the interface permeability condition, we considered only two limiting cases of  $\kappa_s = 0$  (i.e., the fully sealed interface) and  $\kappa_s = \infty$  (i.e., the fully open interface) here. In all figures, the fully sealed interface condition ( $\kappa_s = 0$ ) is presented by a solid curve and the fully open interface condition ( $\kappa_s = \infty$ ) is presented by a dashed curve.

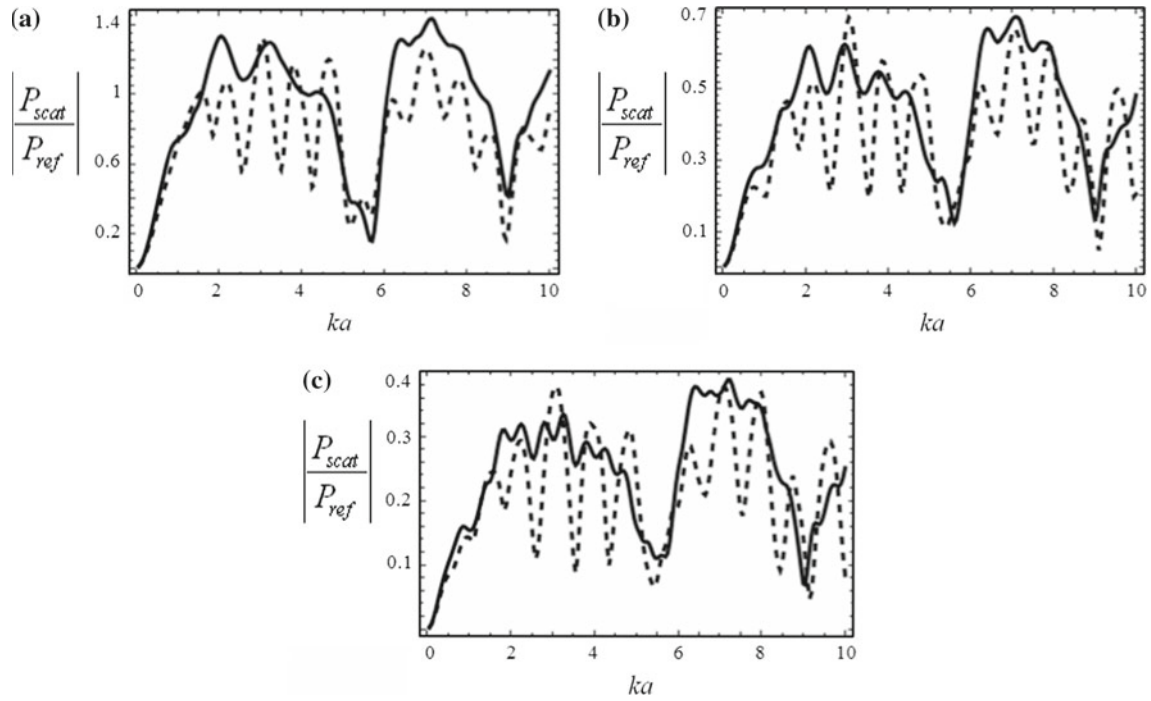
Figure 2 shows the variations of the relative backscattered pressure as functions of non-dimensional frequency ( $ka$ ) for ( $d = 5a, \theta = \pi, Z = 0$ ) and for different radial coordinates of the field point. The most important observations are as follows: Increasing the excitation frequency leads to increasing the backscattered pressure magnitude. The observed oscillatory behavior of the backscattered pressure is due to the acoustic scattering resonances of the porous cylinder. There are two dominating resonances related to eigenfrequencies of the porous cylinder, and the high permeability causes more oscillations on the scattered pressure (the dashed curve is more oscillatory than the solid curve). A general pattern related to the effect of the interface permeability condition on the backscattered pressure is observed in Fig. 2. At low-frequency range ( $0 < ka < 0.56$ ), the effect of the permeability is not noticeable, and two curves coincide with each other. With increasing the frequency to higher range ( $0.56 < ka < 6$ ), the distinction between two cases is noticeable and increasing the permeability of the porous cylinder causes a remarkable decrease in the backscattered pressure. When the first dominated resonance occurs, the backscattered pressure reduces to its minimum and the effect of the permeability diminishes and this pattern continues again at the frequency range  $6 < ka < 9$ . Also the backscattered pressure decreases rapidly with increasing radial coordinates of the field point.

Figure 3 shows angular distributions of the scattered pressure for  $D$  ( $d = 5a, R = 3a, Z = 0$ ) and selected non-dimensional frequencies ( $ka = 0.1, 1, 10$ ). It is obvious that at low frequencies the permeability has not a notable effect on the scattered pressure, while at medium and high frequencies it has a significant effect on reducing the scattered pressure. In addition, it causes the oscillatory behavior of the scattered pressure at high frequencies.

In Fig. 4, the effect of the source to cylinder distance ( $d$ ) on the backscattered pressure is illustrated for  $D$  ( $R = 3a, \theta = \pi, Z = 0$ ) and selected non-dimensional frequencies ( $ka = 0.1, 1, 10$ ). It is clear that increasing the distance between the point source and the cylinder leads to a decrease in the backscattered pressure, while at large distances from the cylinder ( $d > 10a$ ) the variation of the backscattered pressure with respect to distance is not remarkable. Furthermore, while at low frequencies the cylinder permeability has not a notable effect on the backscattered pressure, its overall influence on the backscattered pressure reduction at medium- and high-frequency range is noticeable. Finally, Fig. 5 illustrates the variations of the relative backscattered pressure with the vertical coordinates of the field point for  $D$  ( $d = 5a, R = 3a, \theta = \pi$ ) and  $ka = 0.5$ . The main observation is that the backscattered pressure decreases oscillatory with increasing vertical coordinates of the field point for both interface permeability conditions.

In order to compare our solution with other physical boundary conditions, we used our general Mathematica code to compute the relative backscattered pressure for two other types of water-saturated soils with distinct frame properties (i.e., soft and stiff soils). This comparison can lead to a better understanding of the effect of soil type on the backscattered pressure from the water-saturated porous cylinder. The input parameter values for two different water-saturated soils, that is, soft soil: unconsolidated sand [44] and stiff soil: Nivelsteiner sandstone [45] are compiled in Table 1.

Figure 6 compares the variations of the relative backscattered pressure with non-dimensional frequency ( $ka$ ) for the case of ( $d = 5a, R = 2a, \theta = \pi, Z = 0, \kappa_s = 0$ ) and for three different types of water-satu-



**Fig. 2** **a** The variations of the relative backscattered pressure with non-dimensional frequency ( $ka$ ) for the case of ( $d = 5a$ ,  $\theta = \pi$ ,  $Z = 0$ ) and selected radial coordinate of the field point  $R = 2a$ . Solid line  $\kappa_s = 0$ , dashed line  $\kappa_s = \infty$ . **b** The variations of the relative backscattered pressure with non-dimensional frequency ( $ka$ ) for the case of ( $d = 5a$ ,  $\theta = \pi$ ,  $Z = 0$ ) and selected radial coordinate of the field point  $R = 5a$ . Solid line  $\kappa_s = 0$ , dashed line  $\kappa_s = \infty$ . **c** The variations of the relative backscattered pressure with non-dimensional frequency ( $ka$ ) for the case of ( $d = 5a$ ,  $\theta = \pi$ ,  $Z = 0$ ) and selected radial coordinate of the field point  $R = 10a$ . Solid line  $\kappa_s = 0$ , dashed line  $\kappa_s = \infty$

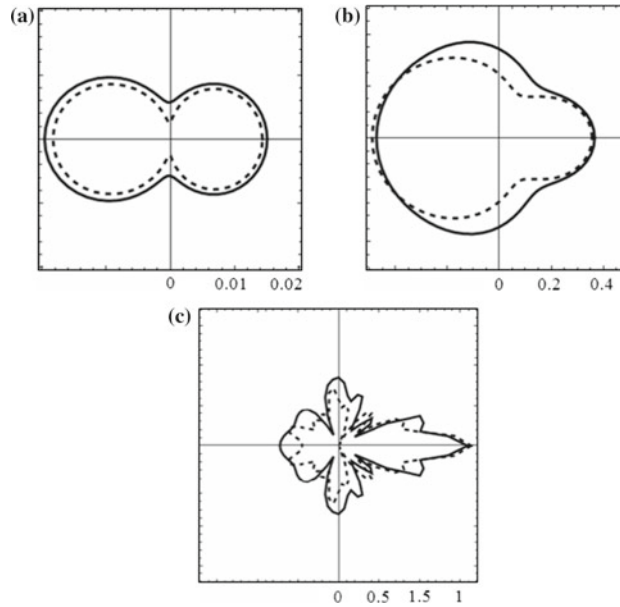


**Fig. 3** **a** The angular distribution of the relative scattered pressure for the case of ( $d = 5a$ ,  $R = 3a$ ,  $Z = 0$ ) and selected non-dimensional frequency  $ka = 0.1$ . Solid line  $\kappa_s = 0$ , dashed line  $\kappa_s = \infty$ . **b** The angular distribution of the relative scattered pressure for the case of ( $d = 5a$ ,  $R = 3a$ ,  $Z = 0$ ) and selected non-dimensional frequency  $ka = 1$ . Solid line  $\kappa_s = 0$ , dashed line  $\kappa_s = \infty$ . **c** The angular distribution of the relative scattered pressure for the case of ( $d = 5a$ ,  $R = 3a$ ,  $Z = 0$ ) and selected non-dimensional frequency  $ka = 10$ . Solid line  $\kappa_s = 0$ , dashed line  $\kappa_s = \infty$

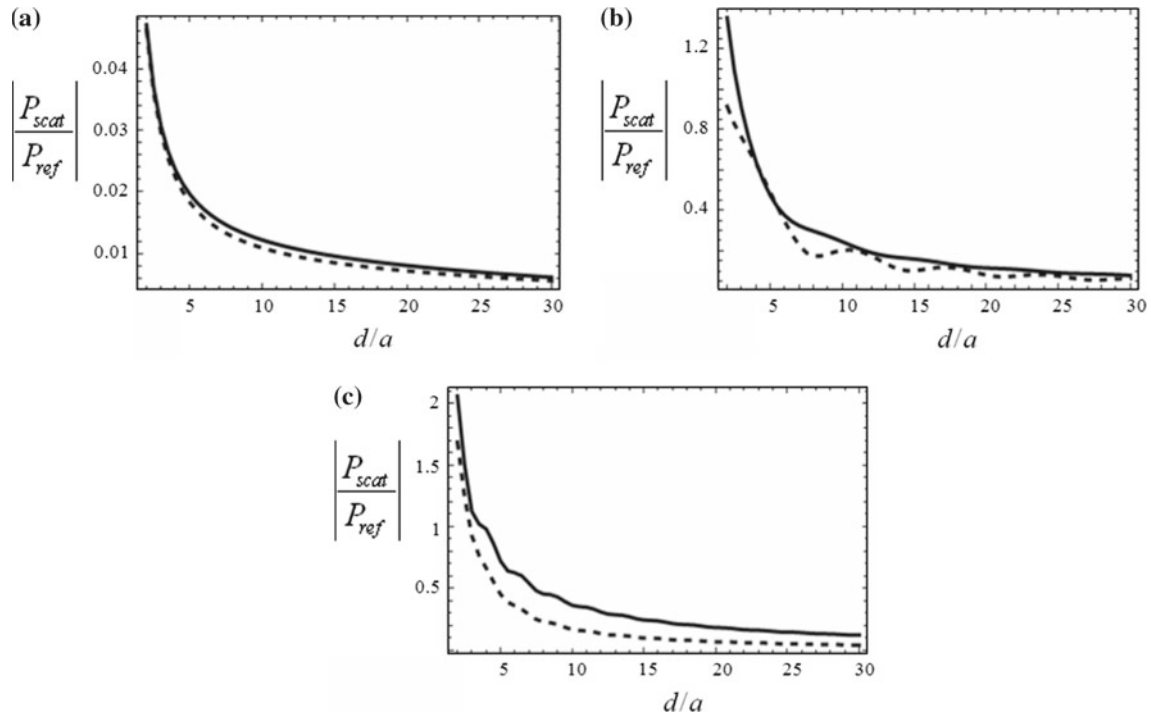


**Fig. 4** **a** The variations of the relative backscattered pressure with distance between source and cylinder for the case of ( $R = 3a, \theta = \pi, Z = 0$ ) and selected non-dimensional frequency  $ka = 0.1$ . Solid line  $\kappa_s = 0$ , dashed line  $\kappa_s = \infty$ . **b** The variations of the relative backscattered pressure with distance between source and cylinder for the case of ( $R = 3a, \theta = \pi, Z = 0$ ) and selected non-dimensional frequency  $ka = 1$ . Solid line  $\kappa_s = 0$ , dashed line  $\kappa_s = \infty$ . **c** The variations of the relative backscattered pressure with distance between source and cylinder for the case of ( $R = 3a, \theta = \pi, Z = 0$ ) and selected non-dimensional frequency  $ka = 10$ . Solid line  $\kappa_s = 0$ , dashed line  $\kappa_s = \infty$

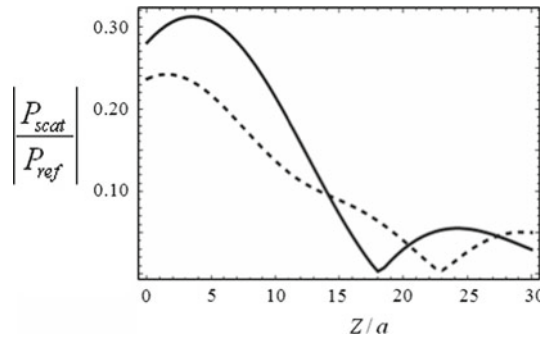


**Fig. 5** The variations of the relative backscattered pressure with vertical coordinates of the field point ( $Z/a$ ) for the case of ( $d = 5a, R = 3a, \theta = \pi, ka = 0.5$ ). Solid line  $\kappa_s = 0$ , dashed line  $\kappa_s = \infty$

rated soils, that is, Ridgefield sandstone (solid curve), unconsolidated sand (dashed curve) and Nivelsteiner sandstone (dash-dotted curve).

As it is obvious, soft soil (dashed curve) exhibits a steady oscillation behavior and decreases the backscattered pressure, while there are sharp oscillations in the backscattered pressure curve associated with stiff soil (dash-dotted curve).

Lastly, in order to verify the overall validity of the work, we used the (all-solid) approximation for the poroelastic cylinder in our general Mathematica code (i.e., we set  $\phi_0 \rightarrow 0, \alpha \rightarrow \infty, \kappa_s = 0, K_{fl} \approx K_0 \approx K_s$  to compute the scattered coefficient for an aluminum cylinder and plotted the real and imaginary parts of  $A_n$  for the mode number ( $n = 0, 1$ ) and non-dimensional frequencies ( $ka = 1, 6$ ) versus longitudinal wave number ( $\zeta$ ). The outcome, as displayed in Fig. 7a, b is in good agreement with the numerical data taken from Fig. 3 of Ref. [29]. For using all-solid approximation in our general Mathematica code, we change the value of the

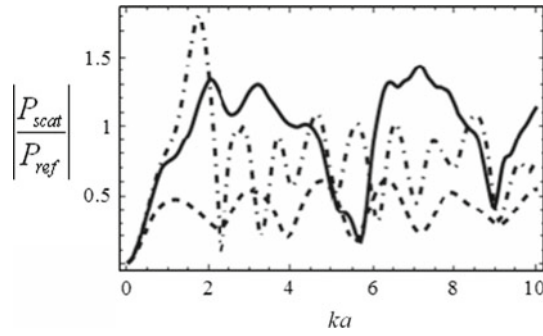


**Fig. 6** The variations of the relative backscattered pressure with non-dimensional frequency ( $ka$ ) for the case of ( $d = 5a$ ,  $R = 2a$ ,  $\theta = \pi$ ,  $Z = 0$ ,  $\kappa_s = 0$ ) and for three different types of water-saturated soils. Ridgefield sandstone (*solid curve*), unconsolidated sand (*dashed curve*) and Nivelsteiner sandstone (*dash-dotted curve*)

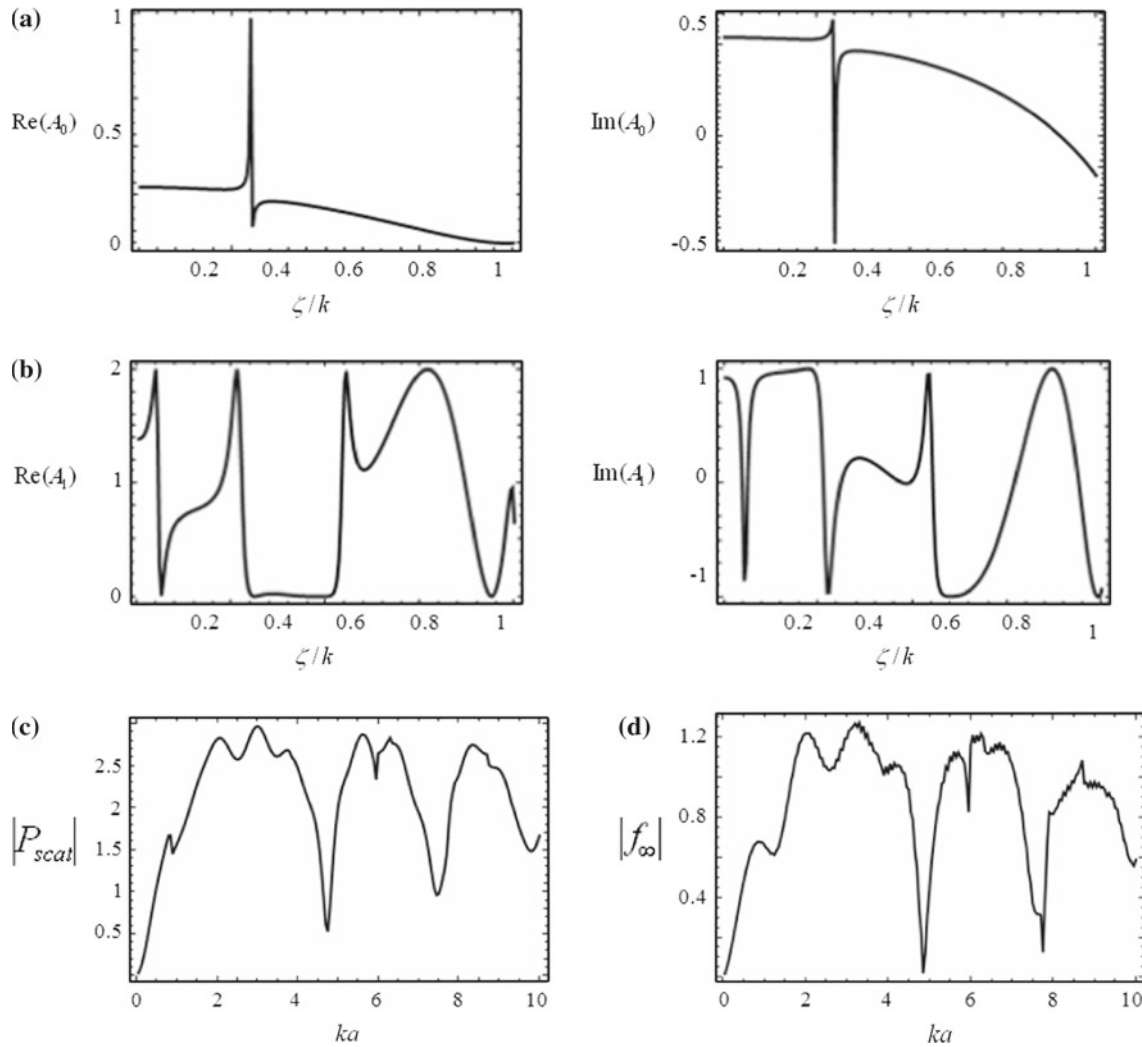


**Fig. 7** **a** The real and imaginary parts of  $A_0$  (the scattering coefficient for the mode number  $n = 0$ ) obtained using the all-solid approximation for the porous cylinder.  $ka = 1$ . **b** The real and imaginary parts of  $A_1$  (the scattering coefficient for the mode number  $n = 1$ ) obtained using the all-solid approximation for the porous cylinder.  $ka = 6$ . **c** The magnitude of the backscattered pressure obtained using the all-solid approximation for the porous cylinder. **d** The magnitude of the form function obtained using the all-solid approximation for the porous cylinder

considered parameters until the optimal convergence is achieved. Or, in other words, until minimizing  $\phi_0$  or maximizing  $\alpha$  does not affect on the scattered pressure. In our code setting  $\phi_0 = 0.001$  and  $\alpha = 10^4$  leads to the optimal convergence of the results without any problem for solving the matrix equation (26).

For further validating, we calculated the backscattered pressure for an elastic solid aluminum cylinder immersed in water and plotted the variations of  $|P_{\text{scat}}|$  with non-dimensional frequency. The outcome, as demonstrated in Fig. 7c, is in good agreement with the numerical data taken from Fig. 5a of Ref. [29]

According to [28], with increasing distance between the spherical wave source and the cylinder ( $d \rightarrow \infty$ ), the obtained results are converged to those obtained for the normal incident plane wave. We considered this fact as another validation test. Again we used all-solid approximation for the poroelastic cylinder in our general Mathematica code to compute the backscattered form function which is defined as [8]  $f_\infty = \sqrt{2R/a} |P_{\text{scat}}|$ , from an elastic solid aluminum cylinder immersed in water. The outcome as shown in Fig. 7d has an acceptable agreement with the form function diagram of normal incident plane waves (Fig. 2 of Ref. [8]).

## 4 Conclusions

Scattering of acoustic spherical waves generated by an immersed monopole point source from an infinitely long fluid-saturated porous cylinder is studied in a closed-form solution. Using a Biot model of dynamic poroelasticity, the translational addition theorem for spherical wave functions, the appropriate wave-field expansions and boundary conditions are utilized to calculate the scattered acoustic field. The most important observations from numerical results are as follows. Increasing the excitation frequency leads to an increase in the backscattered pressure magnitudes, and two dominating frequencies can be observed clearly in the oscillatory curves of the backscattered pressure which is related to the resonances of the porous cylinder. The interface permeability has a significant effect on the reduction in the scattered pressure magnitudes at intermediate and high frequencies, while its overall influence sharply diminishes as the excitation frequency decreases. Also, it causes more oscillatory behavior on the backscattered pressure at intermediate- and high-frequency ranges. The backscattered pressure decreases rapidly by increasing the distance between the source and the cylinder, and increasing the radial and vertical coordinates of the field point leads to a decrease in the backscattered pressure magnitude. Soft soil exhibits a steady oscillation behavior and decreases the backscattered pressure in comparison with stiff soil.

The presented model can lead to a better understanding of three dimensional acoustic scattering from cylindrical targets with poroelastic formations which are commonly encountered in underwater acoustics, seismology, biomechanics, geophysics and noise control engineering, also the obtained results can be used as a benchmark for comparison with other solutions obtained by numerical approximation techniques.

## Appendix

$$\begin{aligned}
 a_{11} &= i\rho_0\omega H_n(\gamma a), \\
 a_{12} &= a_f k_f^2 J_n(\gamma_f a) + 2\mu\gamma_f^2 J_n''(\gamma_f a), \\
 a_{13} &= a_s k_s^2 J_n(\gamma_s a) + 2\mu\gamma_s^2 J_n''(\gamma_s a), \\
 a_{14} &= i2\mu\zeta\gamma_t^2 J_n''(\gamma_t a), \\
 a_{15} &= \frac{2\mu n}{a^2} [\gamma_t a J_n'(\gamma_t a) - J_n(\gamma_t a)], \\
 c_1 &= \frac{\rho_0\omega Q_s}{8\pi} (-1)^n \varepsilon_n J_n(\gamma a) H_n(\gamma d), \\
 a_{21} &= i\rho_0\omega\kappa_s H_n(\gamma a), \\
 a_{22} &= i(1 - \mu_f)\omega\phi_0\gamma_f J_n'(\gamma_f a) - \kappa_s b_f M k_f^2 J_n(\gamma_f a), \\
 a_{23} &= i(1 - \mu_s)\omega\phi_0\gamma_s J_n'(\gamma_s a) - \kappa_s b_s M k_s^2 J_n(\gamma_s a), \\
 a_{24} &= \omega\phi_0\zeta\gamma_t J_n'(\gamma_t a)(\alpha_0 - 1), \\
 a_{25} &= \frac{i\omega\phi_0 n}{a} J_n(\gamma_t a)(1 - \alpha_0),
 \end{aligned}$$

$$\begin{aligned}
c_2 &= \frac{\rho_0 \omega Q_s}{8\pi} (-1)^n \varepsilon_n \kappa_s J_n(\gamma a) H_n(\gamma d), \\
a_{31} &= -\gamma H'_n(\gamma a), \\
a_{32} &= i\omega \gamma_f J'_n(\gamma_f a) [\phi_0(1 - \mu_f) - 1], \\
a_{33} &= i\omega \gamma_s J'_n(\gamma_s a) [\phi_0(1 - \mu_s) - 1], \\
a_{34} &= \omega \zeta \gamma_t J'_n(\gamma_t a) [1 - \phi_0(1 - \alpha_0)], \\
a_{35} &= \frac{i\omega n}{a} J_n(\gamma_t a) [\phi_0(1 - \alpha_0) - 1], \\
c_3 &= \frac{iQ_s}{8\pi} (-1)^n \varepsilon_n \gamma J'_n(\gamma a) H_n(\gamma d), \\
a_{42} &= 2n[J_n(\gamma_f a) - \gamma_f a J'_n(\gamma_f a)], \\
a_{43} &= 2n[J_n(\gamma_s a) - \gamma_s a J'_n(\gamma_s a)], \\
a_{44} &= i2n\zeta[J_n(\gamma_t a) - \gamma_t a J'_n(\gamma_t a)], \\
a_{45} &= -\gamma_t^2 a^2 J''_n(\gamma_t a) + \gamma_t a J'_n(\gamma_t a) - n^2 J_n(\gamma_t a), \\
a_{52} &= i2\zeta \gamma_f a^3 J'_n(\gamma_f a), \\
a_{53} &= i2\zeta \gamma_s a^3 J'_n(\gamma_s a), \\
a_{54} &= -\gamma_t^3 a^3 J'''_n(\gamma_t a) - \gamma_t^2 a^2 J''_n(\gamma_t a) + (-\zeta^2 a^2 + 1 + n^2) \gamma_t a J'_n(\gamma_t a) - 2n^2 J_n(\gamma_t a), \\
a_{55} &= ina^2 \zeta J_n(\gamma_t a).
\end{aligned}$$

## References

1. Faran, J.J.: Sound scattering by solid cylinders and spheres. *J. Acoust. Soc. Am.* **23**, 405–418 (1951)
2. Sodagar, S., Honarvar, F., Sinclair, A.N.: Multiple scattering of an obliquely incident plane acoustic wave from a grating of immersed cylindrical shells. *Appl. Acoust.* **10**, 1–10 (2011)
3. Maze, G., Leon, F., Veksler, N.D.: Scattering of an obliquely incident plane acoustic wave by a circular cylindrical shell: experimental results. *Acta Acustica United with Acustica* **84**, 1–11 (1998)
4. Honarvar, F., Sinclair, A.N.: Scattering of an obliquely incident plane wave from a circular clad rod. *J. Acoust. Soc. Am.* **102**, 41–48 (1997)
5. Leon, F., Chati, F., Conoir, J.M.: Acoustic scattering by an elastic elliptic cylinder in water: numerical results and experiments. *Ultrasonics* **42**, 297–300 (2004)
6. Prospathopoulos, A.M., Athanassoulis, G.A., Belibassakis, K.A.: Underwater acoustic scattering from a radially layered cylindrical obstacle in a 3D ocean waveguide. *J. Sound Vib.* **319**, 1285–1300 (2009)
7. Flax, L., Varadan, V.K., Varadan, V.V.: Scattering of an obliquely incident acoustic wave by an infinite cylinder. *J. Acoust. Soc. Am.* **68**, 1832–1835 (1980)
8. Li, T., Ueda, M.: Sound scattering of a plane wave obliquely incident on a cylinder. *J. Acoust. Soc. Am.* **86**, 2363–2368 (1989)
9. Ahmad, F., Rahman, A.: Acoustic scattering by transversely isotropic cylinders. *Int. J. Eng. Sci.* **38**, 325–335 (2000)
10. Honarvar, F., Sinclair, A.N.: Acoustic wave scattering from transversely isotropic cylinders. *J. Acoust. Soc. Am.* **100**, 57–63 (1996)
11. Fan, Y., Honarvar, F., Sinclair, A.N., Jafari, M.R.: Circumferential resonance modes of solid elastic cylinders excited by obliquely incident acoustic waves. *J. Acoust. Soc. Am.* **113**, 102–113 (2003)
12. Williams, K.L., Kargl, S.G., Thorsos, E.I., Burnett, D.S., Lopes, J.L., Zampolli, M., Marston, P.L.: Acoustic scattering from a solid aluminum cylinder in contact with a sand sediment: measurements, modeling and interpretation. *J. Acoust. Soc. Am.* **127**, 3356–3371 (2010)
13. Calvo, D.C., Rudd, K.E., Zampolli, M., Sanders, W.M., Bibee, L.D.: Simulation of acoustic scattering from an aluminum cylinder near a rough interface using the elastodynamic finite integration technique. *Wave Motion* **47**, 616–634 (2010)
14. Lee, D.S.: Scattering of an incident acoustic wave by an infinite elastic cylinder in a shallow sea. *Math. Methods Appl. Sci.* **32**, 757–772 (2009)
15. Mitri, F.G.: Acoustic backscattering enhancements resulting from the interaction of an obliquely incident plane wave with an infinite cylinder. *Ultrasonics* **50**, 675–682 (2010)
16. Mechel, F.P.: Absorption cross section of absorber cylinders. *J. Sound Vib.* **107**, 131–148 (1986)
17. Laperre, J., Thys, W.: Scattering of ultrasonic waves by an immersed porous cylinder. *Acoust. Lett.* **16**, 9–16 (1992)
18. Umnova, O., Attenborough, K., Linton, C.M.: Effects of porous covering on sound attenuation by periodic arrays of cylinders. *J. Acoust. Soc. Am.* **119**, 278–284 (2006)
19. Hasheminejad, S.M., Avazmohammadi, R.: Acoustic diffraction by a pair of poroelastic cylinders. *ZAMM J. Appl. Math. Mech. Zeitschrift für Angewandte Mathematik und Mechanik* **86**, 589–605 (2006)



20. Hasheminejad, S.M., Alibakhshi, M.A.: Diffraction of sound by a poroelastic cylindrical absorber near an impedance plane. *Int. J. Mech. Sci.* **49**, 1–12 (2007)
21. Gatmiri, B., Eslami, H.: Wave scattering in cross-anisotropic porous media around the cavities and inclusions. *Soil Dyn. Earthq. Eng.* **28**, 1014–1027 (2008)
22. Zhou, X.-L., Wang, J.-H., Xu, B., Jiang, L.-F.: Dynamic response of a circular pipeline in a poroelastic medium. *Mech. Res. Commun.* **36**, 898–905
23. Sebaa, N., Fellah, Z.E.A., Fellah, M., Ogam, E., Wirgin, A., Mitri, F.G., Depollier, C., Lauriks, W.: Ultrasonic characterization of human cancellous bone using the Biot theory: inverse problem. *J. Acoust. Soc. Am.* **120**, 1818–1824 (2006)
24. Ogam, E., Depollier, C., Fellah, Z.E.A.: The direct problem of acoustic diffraction of an audible probe radiation by an air-saturated porous cylinder. *J. Appl. Phys.* **108**, 113519 (2010). doi:[10.1063/1.3514546](https://doi.org/10.1063/1.3514546)
25. Ogam, E., Depollier, C., Fellah, Z.E.A.: The direct and inverse problems of an air-saturated porous cylinder submitted to acoustic radiation. *Rev. Sci. Instrum.* **81**, 094902 (2010). doi:[10.1063/1.3482015](https://doi.org/10.1063/1.3482015)
26. Ogam, E., Fellah, Z.E.A.: The direct and inverse problems of an air-saturated porous cylinder submitted to acoustic radiation. *AIP Adv.* **1**, 032174 (2011). doi:[10.1063/1.3647619](https://doi.org/10.1063/1.3647619)
27. Osman, A.S., Randolph, M.F.: Response of a solid infinite cylinder embedded in a poroelastic medium and subjected to a lateral load. *Int. J. Solids Struct.* **47**, 2414–2424 (2010)
28. Piquette, J.C.: Spherical wave scattering by an elastic solid cylinder of infinite length. *J. Acoust. Soc. Am.* **79**, 1248–1259 (1986)
29. Li, T., Ueda, M.: Sound scattering of a spherical wave incident on a cylinder. *J. Acoust. Soc. Am.* **87**, 1871–1879 (1990)
30. Sheng, J., Alex, E.H.: Spherical wave backscatter from straight cylinders: thin-wire standard targets. *J. Acoust. Soc. Am.* **94**, 2756–2765 (1993)
31. Lui, W.K., Li, K.M.: The scattering of sound by a long cylinder above an impedance boundary. *J. Acoust. Soc. Am.* **127**, 664–674 (2010)
32. Chen, J.-T., Lee, Y.-T., Lin, Y.-J., Chen, I.-L., Lee, J.-W.: Scattering of sound from point sources by multiple circular cylinders using addition theorem and superposition technique. *Numer. Methods Partial Differ. Equ.* **27**, 1365–1383 (2011)
33. Hasheminejad, S.M., Hosseini, H.: Dynamic interaction of a spherical radiator in a fluid-filled cylindrical borehole within a poroelastic formation. *Mech. Res. Commun.* **35**, 158–171 (2008)
34. Hasheminejad, S.M., Hosseini, H.: Nonaxisymmetric interaction of a spherical radiator in a fluid-filled permeable borehole. *Int. J. Solids Struct.* **45**, 24–47 (2008)
35. Achenbach, J.D.: *Wave Propagation in Elastic Solids*. North-Holland, New York (1976)
36. Biot, M.A.: Theory of propagation of elastic waves in a fluid-saturated porous solid I, low-frequency range. *J. Acoust. Soc. Am.* **28**, 168–178 (1956)
37. Biot, M.A.: Theory of propagation of elastic waves in a fluid-saturated porous solid II, high-frequency range. *J. Acoust. Soc. Am.* **28**, 179–191 (1956)
38. Bourbie, T., Coussy, O., Zimmer, B.E.: *Acoustics of Porous Media*. Gulg Publishing, Houston (1987)
39. Wilmanski, K.: A few remarks on Biot's model and linear acoustics of poroelastic saturated materials. *Soil Dyn. Earthq. Eng.* **26**, 509–536 (2006)
40. Johnson, D.L., Koplik, J., Dashen, R.: Theory of dynamic permeability and tortuosity in fluid-saturated porous media. *J. Fluid Mech.* **76**, 379–402 (1987)
41. Johnson, D.L., Plona, T.J., Kojima, H.: Probing porous media with first and second sound, II. Acoustic properties of water saturated porous media. *J. Appl. Phys.* **76**, 115–125 (1994)
42. Abramowitz, M., Stegun, I.: *Handbook of Mathematical Functions*. National Bureau of Standards, Washington DC (1964)
43. Honarvar, F., Sinclair, A.N.: Improvements to the mathematical model of acoustic wave scattering from transversely isotropic cylinders. *Scientia Iranica* **17**, 157–166 (2010)
44. Lo, W.C., Sposito, G., Majer, E.: Low-frequency dilatational wave propagation through fully-saturated poroelastic media. *Adv. Water Resour.* **29**, 408–416 (2006)
45. Carcione, J.M., Cavallini, F., Santos, J.E., Ravazzoli, C.L., Gauzellino, P.M.: Wave propagation in partially saturated porous media, simulation of a second slow wave. *Wave Motion* **39**, 227–240 (2004)